THE JOURNAL OF PHYSICAL CHEMISTRY B



Article

# Bacterial Model Membranes Deform (resp. Persist) Upon Ni Binding to Inner Core (resp. O-Antigen)

HanByul Chang, Karthikeyan Gnanasekaran, Nathan C. Gianneschi, and Franz M. Geiger

*J. Phys. Chem. B*, **Just Accepted Manuscript** • DOI: 10.1021/acs.jpcb.9b02762 • Publication Date (Web): 28 Apr 2019



ACS Publications

is published by the American Chemical Society. 1155 Sixteenth Street N.W., Washington, DC 20036

# Bacterial Model Membranes Deform (*resp*. Persist) Upon $Ni^{2+}$ Binding to Inner Core (*resp*. O-Antigen)

HanByul Chang, Karthikeyan Gnanasekaran, Nathan C. Gianneschi*, and Franz M. Geiger*

Department of Chemistry, Northwestern University, 2145 Sheridan Road, Evanston, IL 60660, USA

**ABSTRACT.** The surface charge densities, apparent equilibrium binding constants, and free energies of binding of nickel ions to supported and suspended lipid membranes prepared from POPC and two types of lipopolysaccharide (LPS) are reported. $2^{nd}$- and $3^{rd}$-order nonlinear optical mixing shows that rough LPS (rLPS)-incorporated bilayers carry the highest charge density and provide the most binding sites for nickel ions while LPS-free bilayers exhibit the lowest charge density and binding sites. $Ni^{2+}$ binding is almost fully reversible at low concentrations but less so at higher $Ni^{2+}$ concentrations. $Ni^{2+}$ adsorption isotherms exhibit hysteresis loops. The role of interfacial depth on the observed second harmonic generation (SHG) responses is discussed in the context of complementary dynamic light scattering, x-ray spectroscopy, and cryogenic transmission electron microscopy experiments. The latter reveal considerable $Ni^{2+}$-induced structural deformations to the bacterial membrane models containing the short, O-antigen-free rLPS, consistent with complex formation on the vesicle surfaces that involve $Ni^{2+}$ ions and carboxylate groups in the inner core of rLPS. In contrast, $Ni^{2+}$ ion complexation to the charged groups (phosphates and carboxylate) of the considerably longer O-antigen units in sLPS appear to protect the phospholipid backbone against metal binding and thus preserve the vesicle structure.

*Corresponding authors: nathan.gianneschi@northwestern.edu and geigerf@chem.northwestern.edu

**I. Introduction.** The incongruent dissolution of lithium ion battery cathode materials, such as lithium cobalt oxide[1,2] and lithium nickel manganese cobalt oxide (NMC),[3-5] has been recently reported to negatively impact uni-[6,7] and multicellular[8,9] organisms upon unintended introduction to the environment. Specifically, bacterial studies studying the impact of NMC on *Shewanella oneidensis* MR-1[6,10] showed that nickel and cobalt ions are mainly responsible for the biological toxicity. Model studies employing lipid bilayers already showed selective affinity of cobalt ions for negatively charged as opposed to zwitterionic lipids,[11] highlighting a need for understanding electrostatically driven membrane-particle interaction with transition metal cations.[12-15] Here, we investigate the interaction of nickel ions, given the previously published toxic impact of nickel, with supported lipid bilayers (SLBs) consisting of the zwitterionic lipid 1-palmitoyl-2-oleoyl-sn-glycero-3-phosphocholine (POPC) and two common types of bacteria-derived lipopolysaccharides (LPS). Our SLBs serve as idealized model systems to understand how bacteria in soil and aquatic environments might interact with and respond to dissolved ions of d-block elements.

LPS, a major component of the outer layer of Gram-negative bacteria,[16] consists of three main components: first, lipid A that is anchored in the surrounding membrane; second, the inner and outer cores which are negatively charged due to carboxylate groups in the sugars located there; and finally, a repeating O-antigen chain made up of polysaccharides. LPS can be further classified as rough LPS (rLPS) that lacks O-antigen repeat units and smooth LPS (sLPS) that varies in the number of O-antigen repeat units depending on the organism.[17,18] The construction of model SLBs with different types of LPS is relevant to understanding bacterial envelopes and is now becoming an emerging field of research.[19-22]

In prior work, we reported that SLBs formed from rLPS-incorporating POPC lipids led to considerably stronger attachment of positive 3-mercaptopropyl amine ($MPNH_2$)-coated gold metal

nanoparticles when compared to SLBs formed from pure POPC, clearly demonstrating the importance of the electrostatic potential produced by the negatively charged groups on the core and O-antigen for adsorption in particle-membrane interactions.[23] Indeed, the charge density on cell membranes has been shown to regulate their interactions with peptides,[24,25] nanomaterials,[15,26] and polymers[27] and is likely to play an important role in LPS-nickel interactions as well. Yet, probing metal cation-membrane interactions real time *in situ*, and without the use of external labels, is not necessarily straightforward, but there are several options, including X-ray photoelectron spectroscopy (XPS),[28,29] scanning probes,[30,31] and fluorescence-based techniques.[32,33] Unlike these methods, nonlinear optical spectroscopic techniques circumvent the requirement for vacuum and/or external labels and yield data in real time and under aqueous flow conditions.

Second harmonic generation (SHG) in particular is widely used to study the interactions of lipid membranes with nanomaterials,[34-37] peptides,[38-41] and ions.[11,42-45] The operational principle is that two photons of the same frequency combine to form one photon of twice the frequency in non-centrosymmetric environments,[46-48] such as liquid/solid interfaces. By mixing the second-order response with the third-order response due to the interfacial potential, $\Phi(0)$, emanating from a charged interface makes the method akin to an "optical voltmeter", with which estimates for surface potentials and interfacial charge densities (and thus metal cation coverage) can be provided. This present work therefore applies this $\Phi(0)$–sensitive form of SHG, also termed the "Eisenthal $\chi^{(3)}$ method"[49-54] to conduct an *in situ*, non-invasive, quantitative analysis of the charge densities of SLBs formed from POPC with and without r- and sLPS, as well as SLBs formed from pure rLPS. We report apparent equilibrium constants and free energies of nickel adsorption to the SLBs and provide estimates for the number density of reversibly and irreversibly adsorbed nickel ions on the bilayers. We pay special attention to the depth-dependent SHG response, given the range in

lengths between the pure POPC (~4 nm bilayer width) and sLPS (7-46 nm length).[55,56] We also evaluate nickel concentration-dependent changes in the size and morphology of vesicles that make up the model bilayers studied in the SHG experiments using dynamic light scattering (DLS) and cryogenic transmission electron microscopy (cryoTEM) and report $Ni^{2+}$-induced LPS-specific deformations of vesicles.

## II. Experimental Methods

**II.A. Laser and Detection System.** Following our previous approach,[26,34,38,57,58] the SHG experiments were conducted using a Ti:sapphire oscillator (Spectra Physics Mai Tai, 82 MHz repetition rate, 120 fs pulse duration) tuned to a fundamental of 800 nm. The beam was attenuated to approximately 0.5 W, polarized parallel to the interface ("s-in"), and focused through a fused silica hemisphere to a diameter of ~30 μm at the fused silica/water interface at an angle just below total internal reflection (~ 60˚). The fundamental and SHG beams exiting the sample (allowing all light polarizations) were passed through a Schott filter and directed into a monochromator set to the second harmonic frequency to remove the fundamental beam. SHG signal was collected using a photomultiplier tube, where the signal was amplified using a gated single-photon detection system.

**II.B. Preparation of Optical Cell and Substrate.** Fused silica hemispheres (ISP Optics, QU-HS-25) were cleaned in NOCHROMIX (Godax Laboratories) cleaning solution for 1 hour and rinsed with ultrapure water (18 MΩ $cm^{-1}$; Millipore, Thermo Scientific). The hemispheres were then sonicated in HPLC-grade methanol for 15 minutes, dried with $N_2$, then air plasma cleaned for 15 minutes on the highest setting, and stored in ultrapure water until use. The custom-built Teflon flow cell used in our experiments has been described in detail before.[59] Briefly, we use creeping flow conditions (2 mL $min^{-1}$) and a shear rate of ~1 mL $min^{-1}$. Prior to each experiment, the cell

was sonicated in methanol for 15 minutes, rinsed with ultrapure water, dried with $N_2$, and then air plasma cleaned for 15 minutes.

**II.C. Buffer, Nickel Solution, and Vesicle Preparation.** 4-(2-hydroxyethyl)-1-piperazineethanesulfonic acid (HEPES) was purchased from Fisher Scientific (powder, purity ≥99%) and NaCl was purchased from Sigma Aldrich. To prepare buffer solutions, appropriate masses of HEPES and NaCl were dissolved into ultrapure water for a final concentration 2 mM HEPES and varying NaCl concentrations used in the experiments. Buffers were then pH adjusted using small aliquots of diluted HCl and NaOH to pH 7.4. Nickel (II) chloride was purchased from Sigma Aldrich (purity >98%) and dissolved in ultrapure water for preparation of stock solution and diluted to the desired concentration in 25 mM NaCl:2 mM HEPES at pH 7.4 for any SHG experiments. Figure S1 shows that the $NiCl_2$ speciation predicted using ChemEQL[60] is dominated to >90% by $Ni^{2+}$ under the conditions of the experiment, with the next most abundant species being singly charged (and thus much less surface active) $NiCl^+$. For all solutions involving $NiCl_2$ solution, we paid special attention so the concentration of NaCl in the final buffered solution does not decrease by more than 95% of the initial concentration due to dilution with $NiCl_2$ solution in pure water.

POPC in chloroform was purchased from Avanti Polar Lipids. rLPS from *Salmonella enterica* serotype minnesota Re 595 (Re mutant) was purchased from Sigma Aldrich as lyophilized powder and suspended in neat chloroform (B&J Brand, HPLC grade) to 2 mg $mL^{-1}$ by sonicating for at least 20 minutes. sLPS from *Salmonella enterica* serotype minnesota purified by phenol extraction was also purchased from Sigma Aldrich as lyophilized powder and suspended in 8:2 methanol/water solution to 2.5 mg $mL^{-1}$ by sonicating for at least 20 minutes. The specific sLPS used in this work has lipid A, core, and up to 20 O-antigen repeat units in the long chain region.[61]

POPC and rLPS were stored at –20 C°, sLPS at –2 C° no longer than 1 month after opening. The chemical structures for POPC and LPS are shown in Scheme 1.[62]

Following our previously published work,[23] we prepared lipid bilayers from unilamellar vesicles containing 80% POPC and 20% LPS (mass ratio). These lipids were mixed for desired ratios in a glass vial, dried under gentle $N_2$ gas, and then dried in vacuum for at least 6 hours. The dried vesicles were then rehydrated in 1 mL 1 mM NaCl:2 mM HEPES at pH 7.4 for at least an hour. Unilamellar lipid vesicles (~100 nm) were prepared by extruding though a 0.05 μm membrane filter (Avanti, 610000) 15 times in 1 mM NaCl:2 mM HEPES at pH 7.4 after 4 cycles of freeze-thaw, 5 minutes each. The vesicles were diluted to 0.5 mg $mL^{-1}$ with appropriate salt concentration for a final buffer concentration of 150 mM NaCl:2 mM HEPES, pH 7.4 immediately before forming SLBs using the vesicle fusion method.[63]

**II.D. Formation of SLBs and Nickel Exposure Experiments.** Following our previously reported procedure,[23] we introduced a solution of 150 mM NaCl:2 mM HEPES at pH 7.4 into the flow cell first and recorded the SHG response in time until a steady signal was attained for at least 10 minutes. Next, extruded vesicles at a concentration of 0.5 mg $mL^{-1}$ in 150 mM NaCl:2 mM HEPES and pH 7.4 were introduced into the cell at a flow rate of 2 mL $min^{-1}$ for two minutes for a total volume of 4 mL (2 flow cell volume equivalents). We then allowed for self-assembly into a lipid bilayer on the fused silica substrate using the vesicle fusion method for at least 30 min (note that the aqueous solution is below the fused silica solid in our flow cell so as to avoid gravitational artifacts). Following bilayer formation, a solution of 150 mM NaCl:2 mM HEPES at pH 7.4 buffer was flushed through the cell at a rate of 2 mL $min^{-1}$ to remove excess vesicles. After a steady SHG signal was observed from the bilayer for at least 20 minutes, the cell was flushed again with a solution of 25 mM NaCl:2 mM HEPES at pH 7.4 buffer at a rate of 2 mL $min^{-1}$ until a steady SHG

signal was again obtained for at least 20 minutes. All nickel exposure experiments were conducted at 25 mM NaCl:2 mM HEPES at pH 7.4. The SHG signal was collected at each nickel and/or NaCl concentration until a steady SHG signal was reached for at least 20 minutes. All SHG experiments were carried out with continuous flow at 2 mL $min^{-1}$ except for the lipid vesicle formation, which happened in static condition.

**II.E. Dynamic Light Scattering.** We determined the hydrodynamic diameter ($d_h$) and zeta ($\xi$) potentials of the extruded vesicles using a Zetasizer Nano ZS instrument (Malvern Instruments, Worcestershire, UK; He-Ne 633 nm laser). Vesicles extruded at 1 mM NaCl:2 mM HEPES at pH 7.4 were diluted to 10 μg $mL^{-1}$ either in 1 mM or 25 mM NaCl with 2 mM HEPES. The values for $d_h$ and $\xi$ potential were determined by averaging three different stock solutions of 30 runs each.

**II.F. Cryogenic Transmission Electron Microscopy (cryoTEM).** Vesicles for cryoTEM were prepared the same way as described in section II.C and $NiCl_2$ stock solutions were directly mixed into the vesicle concentration of 2mg $mL^{-1}$ for the desired final $NiCl_2$ concentration and vortexed for five seconds to aid in mixing. The concentrations of stock nickel solution used for mixing with the vesicles did not change the results between 10 to 100 times dilution. The mixed solution was made about 30 minutes prior to vitrification and 4 μL of the mixture was vitrified using a Vitrobot Mark III, Thermo Fischer Scientific Inc. 200 mesh copper TEM grids with lacey carbon support layer were surface plasma treated before the vitrification procedure using a PELCO easiGlow glow discharge cleaning system. The cryoTEM experiments were performed on a Jeol ARM300F (300 keV) with a cryo holder and transfer station (Gatan Inc., USA) operating at ~ – 170 °C.

**III. Results and Discussion.**

**III.A. CryoTEM Images and DLS Measurements Point Towards a Protective Role of the LPS O-Antigen Against $Ni^{2+}$ Binding.** The hydrodymanic diameter ($d_h$) and zeta ($\xi$) potential of

extruded vesicles measured by DLS (Table 1) indicate the vesicle sizes are slightly smaller in 25 mM NaCl than in 1 mM NaCl, as expected due to screening. CryoTEM images confirm the formation of uniformly sized vesicles with sizes that correspond well with the DLS measurements (Figs. 1A-D, *n.b.*: vesicles were not prepared from pure sLPS). Adding nickel results in higher $d_h$ (Fig. 2A) and more positive $\xi$ potential (Fig. 2B), consistent with nickel ion adsorption onto the vesicles, and indicating vesicle aggregation observed by cryoTEM as described below. The measurements also show that vesicles formed from the 8:2 mix of POPC:rLPS are more susceptible to size changes by nickel binding than vesicles prepared from pure POPC. Nickel ion adsorption also appears to lead to charge reversal, as evidenced by the $\xi$ potential measurements, again most pronounced for the vesicles containing rLPS. This result points to the significant increase in negative charge of rLPS vs POPC (Table 1). High nickel concentrations also lead to the appearance of a second distribution peak of considerably larger size than the first (majority) (Fig. S4).

Our findings are recapitulated in cryoTEM images, which show nickel-induced changes for rLPS and 8:2 POPC:rLPS vesicles in vesicle polydispersity, aggregation, and morphology, particularly at higher nickel concentrations (Figs. 1A'-B"). In contrast, changes in vesicle size and electrostatics are not observed for POPC due to low electrostatic interactions (low surface charge as evidenced by Fig. 2B) or 8:2 POPC:sLPS even at the higher concentration of nickel (Figs. 2B, 1C'-D"), pointing towards a protective role of the O-antigen with regards to $Ni^{2+}$ adsorption.

While these studies are the first that probe how a transition metal cation interacts with the Gram-negative membrane component LPS, heavy metal cation interactions with single-component lipid membranes as well as membrane-trafficking proteins have certainly been studied in much detail. For instance, Garcia and Godwin reported that 1 mM $Pb^{2+}$ and 5 mM $Ca^{2+}$ induce self-

assembly of members of the synaptotagmin (syt) family of vesicle proteins.[64] Other works suggest irregular cation adsorption in protein systems attributed to a combination of chemisorption and physisorption.[65-67] However, in our work, nickel complex formation through chemisorption is minor from the fact that nickel adsorption is at least 90% reversible under most conditions as described later in the main text.

Furthermore, we understand that the deformation of a membrane not only relates to the hydrophilic surface, but also on the order of the hydrophobic tails. Our prior work[11] investigating the interactions of DMPC and 9:1 DMPC/DMPG with another divalent cation, $Co^{2+}$, showed bilayer asymmetry induction by elevated $Co^{2+}$ concentrations for 9:1 DMPC/DMPG. This was explained by specific electrostatic interaction of negatively charged headgroups of the lipid bilayers with positive ions based on the fact that no significant alteration in the bilayer SFG spectra were observed for the zwitterionic DMPC. This induction of lipid asymmetry by metal adsorption was also reported by Conboy[68] and Chen[69] groups for short peptides. We also reported that polycation binding to bilayers resulted in a complete disappearance of the VSFG responses from the well-ordered alkyl chains.[70] Further understanding metal cation binding to the more considerably complicated LPS containing bilayers is certainly of interest but beyond the scope of this work.

**III.B. Small Amounts of rLPS Increase the Membrane Charge Density Considerably.** In addition to cryoTEM, we attempted to quantify nickel concentration in the vesicles by Energy Dispersive X-ray Spectroscopy (EDS). Unfortunately, the low signal to noise ratio of nickel in cryogenic environment prevented us from yielding representative quantification. Therefore, we proceeded to provide $Ni^{2+}$ surface coverage estimates by using the Eisenthal $\chi^{(3)}$ method. These experiments are comprised of two steps: first, the interfacial charge densities of the bare

membranes are estimated by screening the Coulombic charges using varying NaCl concentrations (no $Ni^{2+}$ present). Then, the measurement is repeated at constant total ionic strength and varying nickel concentrations. We note that our analysis includes the required phase matching correction step[49,50,71] as described in the SI Section IX.

Figure 3A shows the SHG charge screening experiments of SLBs prepared from POPC and 8:2 POPC:rLPS. Since POPC is a zwitterionic lipid with zero net charge but slight charge polarization in the head group,[72] we expect the interfacial charge density to be minor. In this case, we use the Gouy-Chapman (GC) model and find an interfacial charge density of $-0.004 \pm 0.002$ C $m^{-2}$. On the other hand, the high charge density expected for rLPS requires the Gouy-Chapman-Stern, or Triple Layer, model (eqn. S1), which consists of a Stern layer near the interface and a diffuse layer extending out into the aqueous phase, as in the GC model.[73,74] We therefore fit the following model to the SHG charge screening data obtained from the bilayer formed from 8:2 POPC:rLPS:

$$I_{SHG} = |E_{SHG}|^2 = \left| A + B \cdot \left\{ -\frac{\sigma_0}{C_2} + \left( 0.0514\ [V] \cdot \sinh^{-1} \frac{\sigma_0\ [C\ m^{-2}]}{0.1174 \left[ C\ m^{-2}\ M^{-\frac{1}{2}} \right] C_{elec}^{\frac{1}{2}}} \right) \right\} \right|^2 \quad \#(1)$$

Here, A and B are constants specific to the terms containing the second- and third-order nonlinear susceptibility tensors, respectively, $C_2$ is the capacitance in the Stern layer, $C_{elec}$ is the electrolyte concentration, and $\sigma_0$ is charge density of the bilayer. Using $C_2 = \varepsilon_0 \varepsilon_{Stern}/\delta$, where $\varepsilon_0$ is the relative permittivity of vacuum ($8.85 \times 10^{-12}$ F $m^{-1}$), $\varepsilon_{Stern} = 100 - 200$,[75,76] and $\delta$ is the Stern layer thickness (5-10 Å), [75-77] $C_2$ is estimated to be 2 to 4 F $m^{-2}$ in this work (The surface under study is diffuse and lacks a molecularly sharp boundary as seen in Scheme 2; the quantities reported in the main text assign the value of 2 F $m^{-2}$ to $C_2$, but values obtained using a range of $C_2$

can be found in Figure S14.) We note that the $\varepsilon_{Stern}$ used above does not refer to the layer of adsorbed ions in the hydration region at the surface. Instead, it refers to the layer at the polar headgroups of the SLB where most of the adsorption occurs. The negatively signed capacitance term retains total charge neutrality. Our analysis shows that $\sigma_{POPC:rLPS} = -0.10 \pm 0.02$ C m$^{-2}$. As expected, rLPS-containing bilayers carry considerably higher negative charge when compared to pure POPC. Scheme 2 provides a simplified working model for some possible binding sites for $Ni^{2+}$ on the rLPS-containing lipid membrane.

**III.F. rLPS-Containing Membranes Bind ~7 x More Nickel than Pure POPC Membranes.** Figure 3B shows the binding curves for $Ni^{2+}$ interaction with the SLBs prepared from pure POPC lipid and those prepared from the 8:2 POPC:rLPS. The SHG responses indicate stronger nickel ion binding for the rLPS-containing bilayers when compared to those prepared from pure POPC. Following the arguments presented in the previous section, we apply the Gouy-Chapman and the Gouy-Chapman-Stern model to the less and more charged membranes, respectively. We use the Langmuir adsorption model,[78] i.e. $\theta = \frac{K_{ads}C}{1 + K_{ads}C}$, where $\theta$, $K_{ads}$ and C are the fractional surface coverage, the apparent equilibrium constant for ion adsorption, and bulk nickel concentration, respectively. Combined with eqn. (S1), we arrive at:

$$E_{SHG} = A + B \cdot 0.0514\ [V] \cdot \sinh^{-1}\left(\left(\sigma_0 + \sigma_{ads,max} \cdot \frac{K_{ads}C}{1 + K_{ads}C}\right) \cdot \left(\frac{1}{0.1174\left[C\, m^{-2}\, M^{-\frac{1}{2}}\right] C_{elec}^{\frac{1}{2}}}\right)\right) \#(2)$$

where $\sigma_0$ and $\sigma_{ads,max}$ are the charge densities of the bare bilayer and the maximum amount of bound ions, respectively. Fitting eqn. (2) to the experimental adsorption isotherms yields surface charge density estimates for $\sigma_{ads,max}$ of 0.019 $\pm$ 0.003 C m$^{-2}$, or 1.2 $\pm$ 0.2 $\times$ $10^{13}$ $Ni^{2+}$ cm$^{-2}$ for

POPC. Moreover, eqn. (2) yields a $K_{ads}$ of $1.4 \pm 0.6 \times 10^{13}$ $M^{-1}$ from which we calculate a $\Delta G_{ads}$ of $-28 \pm 1$ kJ $mol^{-1}$, referenced to the molarity of water, 55 M, at room temperature.

As discussed above, more highly charged bilayers such as those formed from the 8:2 mix of POPC:rLPS require the use of an additional capacitance term. Thus, combining the Langmuir model with eqn. (1), we find

$$E_{SHG} = A + B \cdot \left[ \left\{ \left( -\frac{1}{C_2} \right) \left( \sigma_0 + \sigma_{ads} \cdot \frac{K_{ads} C}{1 + K_{ads} C} \right) \right\} + 0.0514\ [V] \cdot \sinh^{-1} \left( \left( \sigma_0 + \sigma_{ads,max} \cdot \frac{K_{ads} C}{1 + K_{ads} C} \right) \cdot \left( \frac{1}{0.1174 \left[ C\, m^{-2}\, M^{-\frac{1}{2}} \right] C_{elec}^{\frac{1}{2}}} \right) \right) \right] \#(3)$$

Fitting eqn. (3) to the adsorption isotherm for nickel to the bilayer formed from the 8:2 POPC:rLPS SLBs yields charge densities of $0.112 \pm 0.002$ C $m^{-2}$ ($6.9 \pm 0.1 \times 10^{13}$ $Ni^{2+}$ $cm^{-2}$) and $K_{ads}$ of $5 \pm 1 \times 10^{14}$ $M^{-1}$ which corresponds to $\Delta G_{ads}$ of $-36.7 \pm 0.5$ kJ $mol^{-1}$. These fit results indicate a much larger propensity for $Ni^{2+}$ to interact with the rLPS-containing POPC bilayer than with the pure POPC bilayer by itself, consistent with the DLS and cryoTEM data discussed earlier. Adsorption isotherms showing the estimated number of nickel ions adsorbed on the bilayers can be found in Figure S11. The same experiments with pure rLPS bilayers have also been conducted and are summarized in the SI.

To explain our findings of enhanced $Ni^{2+}$ binding to the rLPS-containing POPC bilayer, we consider possible adsorption sites for the divalent nickel cations in rLPS, which are likely to be the carboxylic acid groups in rLPS that are deprotonated at pH 7.4.[79] When we incorporate rLPS into the bilayer, the long chain of rLPS protrudes out of the POPC bilayer,[80] exposing the charged carboxylate moieties for nickel interaction. Nickel ions bind to carboxylate in a monodentate form per carboxylate group,[81] leading to a direct contact ion pair involving the C–$O^-$ group and not the carbonyl group. Following our previously published work,[82] the free energy

associated with the deprotonation of a carboxylic head group ($\Delta G_{dep} = 41 \pm 6\ kJ\ mol^{-1}$) needs to be accounted for in the observed total free energy of adsorption, according to

$$\Delta G_{ads,obs} = \Delta G_{deprotonation} + \Delta G_{M-COO} \#(4A)$$

$$\Delta G_{M-COO} = \Delta G_{ad,obs} - 41 \pm 6\ kJ\ mol^{-1} = -77.7 \pm 6.0\ kJ\ mol^{-1}\ \#(4B)$$

Further, the metal-carboxylate free energy of interaction should be multiplied by 2 if one were to account for 2:1 stoichiometry of the carboxylate:$Ni^{2+}$ complex, resulting in a free energy of rLPS-$Ni^{2+}$ interaction of -155 kJ $mol^{-1}$.

**III.F. Interfacial Depth Probed by the SHG $\chi^{(3)}$ Method.** The membranes studied here can help elucidate some interesting features of the SHG process. The sLPS used in this study consists of at least 20 repeat units of the O-antigen (composed of sugar moieties and negatively charged groups) such that significantly higher charge and more nickel ion binding sites are present in them when compared to the (much shorter) rLPS (Scheme 1). Yet, applying the Gouy-Chapman-Stern model described above to the isotherms shown in Figure 3 yields a charge density for the bilayer formed from the 8:2 mix of POPC:sLPS (-0.03 $\pm$ 0.01 C $m^{-2}$) that is 3 times below that of the rLPS-containing POPC bilayer, while the $Ni^{2+}$ charge density is 0.039 $\pm$ 0.002 C $m^{-2}$ (2.4 $\pm$ 0.1 $\times$ $10^{13}$ $Ni^{2+}$ $cm^{-1}$), also 3 times below that of the rLPS-containing membrane. The $K_{ads}$ for $Ni^{2+}$ adsorption to the 8:2 POPC:sLPS membrane is estimated to be 3.2 $\pm$ 0.8 $\times$ $10^3$ $M^{-1}$, leading to a $\Delta G_{ads}$ for $Ni^{2+}$ adsorption (discounting deprotonation for simplicity) of $-30.0 \pm 0.6$ kJ $mol^{-1}$, ~2kT smaller than that for the POPC:rLPS membrane. This unexpected result could be rationalized by the apparent differences in nickel ion interactions with rLPS- and sLPS-containing vesicles as observed by the cryoTEM images (Figs. 1B'-D''), especially the possible protective role that the O-antigen appears to play in guarding against nickel adsorption on the vesicles.

This counterintuitive result was reported in our earlier study investigating the association of positively charged $MPNH_2$-functionalized gold nanoparticles (AuNPs) with POPC and LPS-incorporated bilayers.[23] In this work, quartz crystal microbalance with dissipation monitoring (QCM-D) showed that O-antigen chain in sLPS presents a larger number of binding sites than rLPS per molecule basis. Additionally, we concluded that the AuNPs interact with the O-antigen domain of the smooth LPS by observing larger contributions to frequency shift and dissipation in lower harmonics (penetrating further into the bulk) than higher harmonics. We also reported that AuNP adsorption on POPC:sLPS induced very little to no changes in SHG, suggesting a clear depth-dependence of SHG.

We also understand that there is much discussion around the topic of interfacial water molecules at varying interfacial depths in the context of nonlinear optical signal generation at aqueous interfaces.[46,49,53,71,83-98] Walker and Richmond showed computationally that water molecules are oriented differently at each distance from the interfacial region and that the net orientation of water molecules contribute to the observed sum frequency generation signal,[99] a result that was recently recapitulated using quantum mechanical calculations.[100,101] Using "molecular rulers", Walker and coworkers reported that interfaces of different composition and lengths can create different interfacial environments by altering the orientation of water molecules, clearly demonstrating the distance dependence of SHG on an Å scale.[102] This dependence could be confirmed by conducting the same experiments with different LPS types with varying O-antigen region length, which is, however, beyond the scope of the current investigation.

**III.G. Reversibility and Hysteresis of $Ni^{2+}$ Binding to Lipid Membranes.** For all three SLBs studied herein, the reversibility of $Ni^{2+}$ adsorption depends on the nickel concentration as shown in Figure 4A for an SLB formed from 8:2 mix of POPC:sLPS as an example. In these experiments,

the membranes were exposed to subsequently increasing nickel concentrations and rinsed with nickel-free buffer between each injection of nickel solution. We observe that the extent of reversibility decreases with increasing $Ni^{2+}$ concentrations. The outcomes are not a function of the sequence of adsorption/desorption cycles, as Figure 4B shows irreversibility even for direct exposure of a freshly prepared membrane to 100 mM $NiCl_2$. The presence of leftover $NiCl_2$ is confirmed by XPS (Fig. 5), albeit *in vacuo* as opposed to *in aquo*.

We also notice step-like features in the SHG vs. time traces recorded while rinsing the rLPS- or sLPS-containing membranes after exposure to nickel (Fig. 4B). This finding suggests the presence of weak binding sites that release $Ni^{2+}$ early on during rinsing, and a second, more strongly binding site. This outcome points to the possibility that the adsorption of nickel is cooperative, where initial nickel adsorption promotes further adsorption. Moreover, the absence of this step-like feature in SHG vs time traces for SLBs formed from pure POPC suggests that the LPS moieties provide higher affinity binding sites for nickel.

Figure 4C reveals hysteresis when $Ni^{2+}$ binds to a membrane formed from an 8:2 mix of POPC:sLPS. Here, the same bilayer is exposed first to increasing (forward arrow) and then decreasing (reverse arrow) nickel ion concentrations. The $Ni^{2+}$ charge density, the binding constants, and the free energies of adsorption for each branch of the hysteresis loop (summarized in Table S2) show no statistically significant differences. However, it is clear that there is a statistically significant difference in the final SHG signal intensity (at the end of the hysteresis loop) once the nickel concentration in solution is returned to the lowest value. The same trend explained so far is observed with POPC and 8:2 POPC:rLPS in varying degrees of reversibility (SI Section VI), with 8:2 POPC:sLPS showing the least extent of reversibility.

**IV. Conclusions.** With the increased use of nanoscale battery materials made from transition metals such as nickel that can pose potential hazards to biological systems, it is critical to understand how these ions interact with biological membranes. In this work, we applied a number of surface-specific *in situ* and *ex situ* techniques to show that rLPS-containing lipid membranes provide a charged environment to which nickel ions can adsorb electrostatically. The interactions are likely to occur via charged moieties at the hydrophilic end of rLPS, forming $Ni^{2+}$-carboxylate complexes. While sLPS has more negatively charged carboxylate binding sites along its O-antigen repeat units than rLPS, its SHG active region is shorter than the length to which it reaches into the bulk aqueous solutions, resulting in incomplete capture of nickel:sLPC interactions by SHG. We have also shown that low nickel concentrations are almost completely reversibly bound to the various membranes, regardless of the presence of LPS. More importantly, high $NiCl_2$ concentrations result in incomplete metal ion desorption upon rinsing and aggregation as well as morphological change observed using DLS and cryoTEM.

Despite the fact that membranes formed from the 8:2 mix of POPC:rLPS exhibit the highest $K_{ads}$ as well as the highest degree of aggregation seen by cryoTEM, these membranes do not show the least extent of reversibility. Surprisingly, it is the 8:2 POPC:sLPS membrane with a comparatively low $K_{ads}$ and no sign of aggregation that exhibits the most irreversible interaction with nickel. The cryoTEM images suggesting a protective role of the O-antigen (Figure 1B") are consistent with the notion that nickel, once adsorbed to the long O-antigen at a long distance away from the lipid membrane, exhibits little influence on the vesicle morphology and properties (size), indicating that the O-antigen has a certain capacity towards $Ni^{2+}$ while retaining its protective role (i.e. no morphology changes). Conversely, and perhaps serving as a counterfactual, LPS-containing vesicles that lack the $Ni^{2+}$-protective O-antigen (formed here from the 8:2 mix of

POPC:rLPS or even pure rLPS) do show morphological changes upon $Ni^{2+}$ binding (Figure 1C" and D").

Taken together, we can speculate that the observed morphology changes are perhaps due to ligand field interactions involving Ni ions bound to two carboxylate groups from one rLPS unit, as pictured in Scheme 2, and a second pair of uncoordinated ($Ni^{2+}$-free) carboxylate groups from a second rLPS unit located in another portion of the membrane. The resulting structures would be reminiscent of multi-nuclear Ni(II) "paddle wheels" in metal organic frameworks reported in the literature.[103] Formation of such "bio-MOFs" on the vesicle surfaces from $Ni^{2+}$ ions and carboxylate groups from O-antigen-free rLPS (Scheme 2) may lead to the folded and bent features observed in cryoTEM images 1C" and D". In contrast, $Ni^{2+}$ ion complexation to the charged groups (phosphates and carboxylate) of the considerably longer O-antigen units in sLPS would protect the phospholipid backbone against metal binding and thus preserve the vesicle structure. The lack of changes to the morphology of the vesicle in cryoTEM images 1B" and the lack of aggregation signaled in the DLS data supports this putative mechanism. Future work is aimed at further studying this process with an eye towards detailed structural studies of possible bio-MOF formation, which are beyond the scope of this present work.

It is our hope that these results may be helpful in providing experimental evidence for understanding the interactions of nickel ions and other transition metals with biological membranes, along with their toxicity towards certain biological systems.[6,10] As we see in this work, the fact that nickel adsorption is only partially reversible provides reason and room for improvement in designing nanoscale materials involving these ions in order to minimize biologically hazardous outcomes. Lastly, we caution that there may be additional factors necessary for more accurate analyses of the experiments presented herein, especially in light of recent

advances in phase-resolved SHG at low ionic strength.[104] Indeed, given that this work utilizes aqueous solutions with ionic strengths of at least 0.6 mM (from HEPES), the DC-field phase shift in the observed optical processes is minimal.[71,86,104-106] Ongoing work is aimed at pursuing metal ion:membrane interactions *in aquo* using liquid-cell transmission electron microscopy (LCTEM) studies of soft-matter interfaces,[107,108] with which investigations aimed at the extent of metal ion binding reversibility are possible.

**V. Associated Content**

Supporting Information: Control experiments. UV-Vis experiments. Additional triplicate DLS and SHG measurements. Additional model fits. Pure 100% rLPS bilayer data.

**VI. Author Information**

Corresponding Author: nathan.gianneschi@northwestern.edu and

geigerf@chem.northwestern.edu

ORCID:

HanByul Chang: 0000-0003-0270-7336

Karthikeyan Gnanasekaran: 0000-0001-6635-0888

Nathan N. Gianneschi: 0000-0001-9945-5475

Franz M. Geiger: 0000-0001-8569-4045

**VII. Acknowledgement.** This work is supported by the National Science Foundation under the Center for Sustainable Nanotechnology, Grant No.CHE-1503408. NCG acknowledges support by a grant from an ARO MURI (W911NF-5-1-0568). K.G. acknowledges support from the Human Frontiers in Science Program (HFSP). FMG acknowledges support from a Dow Chemical Company Professorship and from the Alexander von Humboldt Foundation.

**References.**

**References.**

1. Xia, H.; Wan, Y.; Assenmacher, W.; Mader, W.; Yuan, G.; Lu, L. Facile Synthesis of Chain-Like $LiCoO_2$ Nanowire Arrays as Three-Dimensional Cathode for Microbatteries. *NPG Asia Mater.* **2014,** *6*, e126.
2. Gulbinska, M. K., *Lithium-Ion Battery Materials and Engineering: Current Topics and Problems from the Manufacturing Perspective*. Springer: London, 2014.
3. Zhang, R.; Xia, B.; Li, B.; Lai, Y.; Zheng, W.; Wang, H.; Wang, W.; Wang, M. Study on the Characteristics of a High Capacity Nickel Manganese Cobalt Oxide (NMC) Lithium-Ion Battery—an Experimental Investigation. *Energies* **2018,** *11* (9), 2275.
4. Kim, Y. Lithium Nickel Cobalt Manganese Oxide Synthesized Using Alkali Chloride Flux: Morphology and Performance as a Cathode Material for Lithium Ion Batteries. *ACS Appl. Mater. Interfaces* **2012,** *4* (5), 2329-2333.
5. Tian, Z.; Yu, H.; Zhang, Z.; Xu, X. Performance Improvements of Cobalt Oxide Cathodes for Rechargeable Lithium Batteries. *ChemBioEng Rev.* **2018,** *5* (2), 111-118.
6. Hang, M. N.; Gunsolus, I. L.; Wayland, H.; Melby, E. S.; Mensch, A. C.; Hurley, K. R.; Pedersen, J. A.; Haynes, C. L.; Hamers, R. J. Impact of Nanoscale Lithium Nickel Manganese Cobalt Oxide (NMC) on the Bacterium *Shewanella oneidensis* MR-1. *Chem. Mater.* **2016,** *28* (4), 1092-1100.
7. Feng, Z. V.; Miller, B. R.; Linn, T. G.; Pho, T.; Hoang, K. N. L.; Hang, M. N.; Mitchell, S. L.; Hernandez, R. T.; Carlson, E. E.; Hamers, R. J. Biological Impact of Nanoscale Lithium Intercalating Complex Metal Oxides to Model Bacterium *B. subtilis*. *Environ. Sci. Nano* **2019,** *6* (1), 305-314.
8. Bozich, J.; Hang, M.; Hamers, R.; Klaper, R. Core Chemistry Influences the Toxicity of Multicomponent Metal Oxide Nanomaterials, Lithium Nickel Manganese Cobalt Oxide, and Lithium Cobalt Oxide to *Daphnia magna*. *Environ. Toxicol. Chem.* **2017,** *36* (9), 2493-2502.
9. Permenter, M. G.; Lewis, J. A.; Jackson, D. A. Exposure to Nickel, Chromium, or Cadmium Causes Distinct Changes in the Gene Expression Patterns of a Rat Liver Derived Cell Line. *PLoS One* **2011,** *6* (11), e27730-e27730.
10. Gunsolus, I. L.; Hang, M. N.; Hudson-Smith, N. V.; Buchman, J. T.; Bennett, J. W.; Conroy, D.; Mason, S. E.; Hamers, R. J.; Haynes, C. L. Influence of Nickel Manganese Cobalt Oxide Nanoparticle Composition on Toxicity toward *Shewanella oneidensis* MR-1: Redesigning for Reduced Biological Impact. *Environ. Sci. Nano* **2017,** *4* (3), 636-646.
11. Doğangün, M.; Hang, M. N.; Machesky, J.; McGeachy, A. C.; Dalchand, N.; Hamers, R. J.; Geiger, F. M. Evidence for Considerable Metal Cation Concentrations from Lithium Intercalation Compounds in the Nano–Bio Interface Gap. *J. Phys. Chem. C* **2017,** *121* (49), 27473-27482.
12. Nel, A. E.; Mädler, L.; Velegol, D.; Xia, T.; Hoek, E. M. V.; Somasundaran, P.; Klaessig, F.; Castranova, V.; Thompson, M. Understanding Biophysicochemical Interactions at the Nano–Bio Interface. *Nat. Mater.* **2009,** *8*, 543.
13. Baca, H. K.; Ashley, C.; Carnes, E.; Lopez, D.; Flemming, J.; Dunphy, D.; Singh, S.; Chen, Z.; Liu, N.; Fan, H., et al. Cell-Directed Assembly of Lipid-Silica Nanostructures Providing Extended Cell Viability. *Science* **2006,** *313*, 337-341.

14. Baca, H. K.; Carnes, E.; Singh, S.; Ashley, C.; Lopez, D.; Brinker, C. J. Cell-Directed Assembly of Bio/Nano Interfaces—a New Scheme for Cell Immobilization. *Acc. Chem. Res.* **2007,** *40* (9), 836-845.
15. Arakha, M.; Saleem, M.; Mallick, B. C.; Jha, S. The Effects of Interfacial Potential on Antimicrobial Propensity of ZnO Nanoparticle. *Sci. Rep* **2015,** *5*, 9578.
16. Cornelissen, C. N.; Fisher, B.D.; Harvey, R. A.*Microbiology*; Harvey, R., Ed.; Lippincott Williams & Wilkins: Philadelphia, 2013; pp 13-52.
17. Lerouge, I.; Vanderleyden, J. O-Antigen Structural Variation: Mechanisms and Possible Roles in Animal/Plant–Microbe Interactions. *FEMS Microbiol. Rev.* **2002,** *26* (1), 17-47.
18. Voet, D. *Biochemistry*. 3rd ed.; J. Wiley & Sons: New York, 2004.
19. Tong, J.; McIntosh, T. J. Structure of Supported Bilayers Composed of Lipopolysaccharides and Bacterial Phospholipids: Raft Formation and Implications for Bacterial Resistance. *Biophys. J.* **2004,** *86* (6), 3759-3771.
20. Kaufmann, S.; Ilg, K.; Mashaghi, A.; Textor, M.; Priem, B.; Aebi, M.; Reimhult, E. Supported Lipopolysaccharide Bilayers. *Langmuir* **2012,** *28* (33), 12199-12208.
21. Snyder, S.; Kim, D.; McIntosh, T. J. Lipopolysaccharide Bilayer Structure: Effect of Chemotype, Core Mutations, Divalent Cations, and Temperature. *Biochemistry* **1999,** *38* (33), 10758-10767.
22. Nomura, K.; Inaba, T.; Morigaki, K.; Brandenburg, K.; Seydel, U.; Kusumoto, S. Interaction of Lipopolysaccharide and Phospholipid in Mixed Membranes: Solid-State $^{31}$P-NMR Spectroscopic and Microscopic Investigations. *Biophys. J.* **2008,** *95* (3), 1226-1238.
23. Jacobson, K. H.; Gunsolus, I. L.; Kuech, T. R.; Troiano, J. M.; Melby, E. S.; Lohse, S. E.; Hu, D.; Chrisler, W. B.; Murphy, C. J.; Orr, G., et al. Lipopolysaccharide Density and Structure Govern the Extent and Distance of Nanoparticle Interaction with Actual and Model Bacterial Outer Membranes. *Environ. Sci. Technol.* **2015,** *49* (17), 10642-10650.
24. Bechinger, B.; Gorr, S.-U. Antimicrobial Peptides: Mechanisms of Action and Resistance. *J. Dent. Res.* **2017,** *96* (3), 254-260.
25. Ciumac, D.; Campbell, R. A.; Xu, H.; Clifton, L. A.; Hughes, A. V.; Webster, J. R. P.; Lu, J. R. Implications of Lipid Monolayer Charge Characteristics on Their Selective Interactions with a Short Antimicrobial Peptide. *Colloids Surf. B* **2017,** *150*, 308-316.
26. Troiano, J. M.; Olenick, L. L.; Kuech, T. R.; Melby, E. S.; Hu, D.; Lohse, S. E.; Mensch, A. C.; Dogangun, M.; Vartanian, A. M.; Torelli, M. D., et al. Direct Probes of 4 nm Diameter Gold Nanoparticles Interacting with Supported Lipid Bilayers. *J. Phys. Chem. C* **2015,** *119* (1), 534-546.
27. McGeachy, A. C.; Dalchand, N.; Caudill, E. R.; Li, T.; Dogangun, M.; Olenick, L.; Chang, H.; Pedersen, J. A.; Geiger, F. Interfacial Electrostatics of Poly(vinylamine hydrochloride), Poly(diallyldimethylammonium chloride), Poly-L-Lysine, and Poly-L-Arginine Interacting with Lipid Bilayers. *Phys. Chem. Chem. Phys.* **2018,** *20*, 10846-10856.
28. Belatik, A.; Hotchandani, S.; Carpentier, R.; Tajmir-Riahi, H.-A. Locating the Binding Sites of Pb(II) Ion with Human and Bovine Serum Albumins. *PLoS One* **2012,** *7* (5), e36723.
29. Karlsson, H. L.; Cronholm, P.; Hedberg, Y.; Tornberg, M.; De Battice, L.; Svedhem, S.; Wallinder, I. O. Cell Membrane Damage and Protein Interaction Induced by Copper Containing Nanoparticles—Importance of the Metal Release Process. *Toxicology* **2013,** *313* (1), 59-69.

30. Redondo-Morata, L.; Oncins, G.; Sanz, F. Force Spectroscopy Reveals the Effect of Different Ions in the Nanomechanical Behavior of Phospholipid Model Membranes: The Case of Potassium Cation. *Biophys. J.* **2012,** *102* (1), 66-74.
31. Redondo-Morata, L.; Giannotti, M. I.; Sanz, F. Structural Impact of Cations on Lipid Bilayer Models: Nanomechanical Properties by AFM-Force Spectroscopy. *Molecular Membrane Biology* **2014,** *31* (1), 17-28.
32. Javanainen, M.; Melcrová, A.; Magarkar, A.; Jurkiewicz, P.; Hof, M.; Jungwirth, P.; Martinez-Seara, H. Two Cations, Two Mechanisms: Interactions of Sodium and Calcium with Zwitterionic Lipid Membranes. *ChemComm* **2017,** *53* (39), 5380-5383.
33. Baumler, S. M.; Blanchard, G. J. The Influence of Metal Ions on the Dynamics of Supported Phospholipid Langmuir Films. *Langmuir* **2017,** *33* (12), 2986-2992.
34. Troiano, J. M.; Kuech, T. R.; Vartanian, A. M.; Torelli, M. D.; Sen, A.; Jacob, L. M.; Hamers, R. J.; Murphy, C. J.; Pedersen, J. A.; Geiger, F. M. On Electronic and Charge Interference in Second Harmonic Generation Responses from Gold Metal Nanoparticles at Supported Lipid Bilayers. *J. Phys. Chem. C* **2016,** *120* (37), 20659-20667.
35. Doğangün, M.; Hang, M. N.; Troiano, J. M.; McGeachy, A. C.; Melby, E. S.; Pedersen, J. A.; Hamers, R. J.; Geiger, F. M. Alteration of Membrane Compositional Asymmetry by $LiCoO_2$ Nanosheets. *ACS Nano* **2015,** *9* (9), 8755-8765.
36. Timbrell, D.; You, J. W.; Kivshar, Y. S.; Panoiu, N. C. A Comparative Analysis of Surface and Bulk Contributions to Second-Harmonic Generation in Centrosymmetric Nanoparticles. *Sci. Rep* **2018,** *8* (1), 3586.
37. Kumal, R. R.; Abu-Laban, M.; Hamal, P.; Kruger, B.; Smith, H. T.; Hayes, D. J.; Haber, L. H. Near-Infrared Photothermal Release of siRNA from the Surface of Colloidal Gold–Silver–Gold Core–Shell–Shell Nanoparticles Studied with Second-Harmonic Generation. *J. Phys. Chem. C* **2018,** *122* (34), 19699-19704.
38. McGeachy, A. C.; Caudill, E. R.; Liang, D.; Cui, Q.; Pedersen, J. A.; Geiger, Franz M. Counting Charges on Membrane-Bound Peptides. *Chem. Sci.* **2018,** *9* (18), 4285-4298.
39. Akkiraju, H.; Moore, M. T.; Srinivasan, P. P.; Kirn Safran, C.; Nohe, A. Use of Second Harmonic Imaging and Fourier Transformation to Analyze Cartilage Repair in Mice Injected with a Novel Peptide CK2.1. *Biophys. J.* **2016,** *110* (3, Supplement 1), 166a.
40. Rao, Y.; Kwok, S. J. J.; Lombardi, J.; Turro, N. J.; Eisenthal, K. B. Label-Free Probe of HIV-1 TAT Peptide Binding to Mimetic Membranes. *Proc. Natl. Acad. Sci. U.S.A.* **2014,** *111* (35), 12684-12688.
41. Ding, B.; Panahi, A.; Ho, J.-J.; Laaser, J. E.; Brooks, C. L.; Zanni, M. T.; Chen, Z. Probing Site-Specific Structural Information of Peptides at Model Membrane Interface in Situ. *J. Am. Chem. Soc.* **2015,** *137* (32), 10190-10198.
42. McCaffrey, D. L.; Nguyen, S. C.; Cox, S. J.; Weller, H.; Alivisatos, A. P.; Geissler, P. L.; Saykally, R. J. Mechanism of Ion Adsorption to Aqueous Interfaces: Graphene/Water Vs. Air/Water. *Proc. Natl. Acad. Sci. U.S.A.* **2017,** *114* (51), 13369-13373.
43. Gan, W.; Wu, W.; Yang, F.; Hu, D.; Fang, H.; Lan, Z.; Yuan, Q. The Behavior of Hydroxide and Hydronium Ions at the Hexadecane–Water Interface Studied with Second Harmonic Generation and Zeta Potential Measurements. *Soft Matter* **2017,** *13* (43), 7962-7968.
44. Song, J.; Kang, T. H.; Kim, M. W.; Han, S. Ion Specific Effects: Decoupling Ion–Ion and Ion–Water Interactions. *Phys. Chem. Chem. Phys.* **2015,** *17* (13), 8306-8322.

45. Holmes, A. M.; Song, Z.; Moghimi, H. R.; Roberts, M. S. Relative Penetration of Zinc Oxide and Zinc Ions into Human Skin after Application of Different Zinc Oxide Formulations. *ACS Nano* **2016,** *10* (2), 1810-1819.
46. Eisenthal, K. B. Second Harmonic Spectroscopy of Aqueous Nano- and Microparticle Interfaces. *Chem. Rev* **2006,** *106* (4), 1462-1477.
47. Ong, S.; Zhao, X.; Eisenthal, K. B. Polarization of Water Molecules at a Charged Interface: Second Harmonic Studies of the Silica/Water Interface. *Chem. Phys. Lett.* **1992,** *191* (3), 327-335.
48. Eisenthal, K. B. Liquid Interfaces Probed by Second-Harmonic and Sum-Frequency Spectroscopy. *Chem. Rev* **1996,** *96* (4), 1343-1360.
49. Ohno, P. E.; Saslow, S. A.; Wang, H.-f.; Geiger, F. M.; Eisenthal, K. B. Phase-Referenced Nonlinear Spectroscopy of the α-Quartz/Water Interface. *Nat. Commun.* **2016,** *7*, 13587.
50. Boamah, M. D.; Ohno, P. E.; Geiger, F. M.; Eisenthal, K. B. Relative Permittivity in the Electrical Double Layer from Nonlinear Optics. *J. Chem. Phys.* **2018,** *148*, 222808.
51. Chen, E. H.; Saslow, S. A.; Nguyen, S. T.; Geiger, F. M. Zinc Ion-Hydroxyl Interactions at Undecanol-Funcationalized Fused Silica/Water Interfaces Quantified Using the Eisenthal $\chi^{(3)}$ Technique. *J. Phys. Chem. C* **2012,** *116*, 19886-19892.
52. Eisenthal, K. B. Second Harmonic Spectroscopy of Aqueous Nano- and Microparticle Interfaces *Chem. Rev.* **2006,** *106*, 1462-1477.
53. Ong, S. W.; Zhao, X. L.; Eisenthal, K. B. Polarization of Water Molecules at a Charged Interface: Second Harmonic Studies of the Silica/Water Interface. *Chem. Phys. Lett.* **1992,** *191* (3-4), 327-335.
54. Zhao, X. L.; Subrahmanyan, S.; Eisenthal, K. B. Determination of pKa at the Air-Water-Interface by 2nd Harmonic-Generation. *Chem. Phys. Lett.* **1990,** *171* (5-6), 558-562.
55. Raetz, C. R. H.; Whitfield, C. Lipopolysaccharide Endotoxins. *Annu. Rev. Biochem.* **2002,** *71*, 635-700.
56. Strauss, J.; Burnham, N. A.; Camesano, T. A. Atomic Force Microscopy Study of the Role of LPS O-Antigen on Adhesion of *E. coli*. *J. Mol. Recognit.* **2009,** *22* (5), 347-355.
57. McGeachy, A. C.; Olenick, L. L.; Troiano, J. M.; Lankone, R. S.; Melby, E. S.; Kuech, T. R.; Ehimiaghe, E.; Fairbrother, D. H.; Pedersen, J. A.; Geiger, F. M. Resonantly Enhanced Nonlinear Optical Probes of Oxidized Multiwalled Carbon Nanotubes at Supported Lipid Bilayers. *J. Phys. Chem. B* **2017,** *121* (6), 1321-1329.
58. Troiano, J. M.; McGeachy, A. C.; Olenick, L. L.; Fang, D.; Liang, D.; Hong, J.; Kuech, T. R.; Caudill, E. R.; Pedersen, J. A.; Cui, Q., et al. Quantifying the Electrostatics of Polycation–Lipid Bilayer Interactions. *J. Am. Chem. Soc.* **2017,** *139* (16), 5808-5816.
59. Gibbs-Davis, J. M.; Kruk, J. J.; Konek, C. T.; Scheidt, K. A.; Geiger, F. M. Jammed Acid-Base Chemistry at Interfaces. *J. Am. Chem. Soc.* **2008,** *130*, 15444-15447.
60. Müller, B. *Chemeql*, 3.0; Limnological Research Center, Swiss Federal Institute of Aquatic Science and Technology: Kastanienbaum, Switzerland, 2005.
61. Peterson, A. A.; McGroarty, E. J. High-Molecular-Weight Components in Lipopolysaccharides of *Salmonella typhimurium, Salmonella minnesota*, and *Escherichia coli*. *J. Bacteriol.* **1985,** *162* (2), 738-745.
62. Bagheri, M.; Keller, S.; Dathe, M. Interaction of W-Substituted Analogs of Cyclo-RRRWFW with Bacterial Lipopolysaccharides: The Role of the Aromatic Cluster in Antimicrobial Activity. *Antimicrob. Agents Chemother.* **2011,** *55* (2), 788-97.

63. Akesson, A.; Lind, T.; Ehrlich, N.; Stamou, D.; Wacklin, H.; Cardenas, M. Composition and Structure of Mixed Phospholipid Supported Bilayers Formed by POPC and DPPC. *Soft Matter* **2012,** *8* (20), 5658-5665.
64. García, R. A.; Godwin, H. A. High Metal Concentrations Are Required for Self-Association of Synaptotagmin II. *Biophys. J.* **2004,** *86* (4), 2455-2466.
65. Medda, L.; Carucci, C.; Parsons, D. F.; Ninham, B. W.; Monduzzi, M.; Salis, A. Specific Cation Effects on Hemoglobin Aggregation Below and at Physiological Salt Concentration. *Langmuir* **2013,** *29* (49), 15350-15358.
66. Carucci, C.; Haltenort, P.; Salazar, M.; Salis, A.; Magner, E. Hofmeister Phenomena in Bioelectrochemistry: The Supporting Electrolyte Affects the Response of Glucose Electrodes. *ChemElectroChem* **2015,** *2* (5), 659-663.
67. Medda, L.; Monduzzi, M.; Salis, A. The Molecular Motion of Bovine Serum Albumin under Physiological Conditions Is Ion Specific. *ChemComm* **2015,** *51* (30), 6663-6666.
68. Brown, K. L.; Conboy, J. C. Electrostatic Induction of Lipid Asymmetry. *J. Am. Chem. Soc.* **2011,** *133* (23), 8794-8797.
69. Casillas-Ituarte, N. N.; Chen, X.; Castada, H.; Allen, H. C. $Na^+$ and $Ca^{2+}$ Effect on the Hydration and Orientation of the Phosphate Group of DPPC at Air−Water and Air−Hydrated Silica Interfaces. *J. Phys. Chem. B* **2010,** *114* (29), 9485-9495.
70. Olenick, L. L.; Troiano, J. M.; Vartanian, A.; Melby, E. S.; Mensch, A. C.; Zhang, L.; Hong, J.; Mesele, O.; Qiu, T.; Bozich, J., et al. Lipid Corona Formation from Nanoparticle Interactions with Bilayers. *Chem* **2018,** *4* (11), 2709-2723.
71. Gonella, G.; Lütgebaucks, C.; de Beer, A. G. F.; Roke, S. Second Harmonic and Sum-Frequency Generation from Aqueous Interfaces Is Modulated by Interference. *J. Phys. Chem. C* **2016,** *120* (17), 9165-9173.
72. Nagata, Y.; Mukamel, S. Vibrational Sum-Frequency Generation Spectroscopy at the Water/Lipid Interface: Molecular Dynamics Simulation Study. *J. Am. Chem. Soc.* **2010,** *132*, 6434-6442.
73. Lee, C.; Petersen, N. The Triple Layer Model: A Different Perspective on Lipid Bilayers. *J. Chin. Chem. Soc.* **2004,** *51* (5B), 1183-1191.
74. Leroy, P.; Revil, A. A Triple-Layer Model of the Surface Electrochemical Properties of Clay Minerals. *J. Colloid Interface Sci.* **2004,** *270* (2), 371-380.
75. Tanizaki, S.; Feig, M. A Generalized Born Formalism for Heterogeneous Dielectric Environments: Application to the Implicit Modeling of Biological Membranes. *J. Chem. Phys.* **2005,** *122* (12), 124706.
76. Stern, H. A.; Feller, S. E. Calculation of the Dielectric Permittivity Profile for a Nonuniform System: Application to a Lipid Bilayer Simulation. *J. Chem. Phys.* **2003,** *118* (7), 3401-3412.
77. Brown, M. A.; Goel, A.; Abbas, Z. Effect of Electrolyte Concentration on the Stern Layer Thickness at a Charged Interface. *Angew. Chem. Int. Ed.* **2016,** *55* (11), 3790-3794.
78. Langmuir, I. The Constitution and Fundamental Properties of Solids and Liquids. Part I. Solids. *J. Am. Chem. Soc.* **1916,** *38* (11), 2221-2295.
79. Schneck, E.; Schubert, T.; Konovalov, O. V.; Quinn, B. E.; Gutsmann, T.; Brandenburg, K.; Oliveira, R. G.; Pink, D. A.; Tanaka, M. Quantitative Determination of Ion Distributions in Bacterial Lipopolysaccharide Membranes by Grazing-Incidence X-Ray Fluorescence. *Proc. Natl. Acad. Sci. U.S.A.* **2010,** *107* (20), 9147-9151.

80. Clifton, L. A.; Skoda, M. W. A.; Daulton, E. L.; Hughes, A. V.; Le Brun, A. P.; Lakey, J. H.; Holt, S. A. Asymmetric Phospholipid: Lipopolysaccharide Bilayers; a Gram-Negative Bacterial Outer Membrane Mimic. *J. Royal Soc. Interface* **2013,** *10* (89), 20130810.
81. Simon-Kutscher, J.; Gericke, A.; Hühnerfuss, H. Effect of Bivalent Ba, Cu, Ni, and Zn Cations on the Structure of Octadecanoic Acid Monolayers at the Air−Water Interface as Determined by External Infrared Reflection−Absorption Spectroscopy. *Langmuir* **1996,** *12* (4), 1027-1034.
82. Malin, J. N.; Hayes, P. L.; Geiger, F. M. Interactions of Ca, Zn, and Cd Ions at Buried Solid/Water Interfaces Studied by Second Harmonic Generation. *J. Phys. Chem. C* **2009,** *113* (6), 2041-2052.
83. Du, Q.; Freysz, E.; Shen, Y. R. Vibrational Spectra of Water Molecules at Quartz/Water Interfaces. *Phys. Rev. Lett.* **1994,** *72* (2), 238-241.
84. Wang, H.; Yan, E. C. Y.; Borguet, E.; Eisenthal, K. B. Second Harmonic Generation from the Surface of Centrosymmetric Particles in Bulk Solution. *Chem. Phys. Lett.* **1996,** *259* (1), 15-20.
85. Shen, Y. R.; Ostroverkhov, V. Sum-Frequency Vibrational Spectroscopy on Water Interfaces: Polar Orientation of Water Molecules at Interfaces. *Chem. Rev* **2006,** *106* (4), 1140-1154.
86. Wen, Y.-C.; Zha, S.; Liu, X.; Yang, S.; Guo, P.; Shi, G.; Fang, H.; Shen, Y. R.; Tian, C. Unveiling Microscopic Structures of Charged Water Interfaces by Surface-Specific Vibrational Spectroscopy. *Phys. Rev. Lett.* **2016,** *116* (1), 016101.
87. Schaefer, J.; Gonella, G.; Bonn, M.; Backus, E. H. G. Surface-Specific Vibrational Spectroscopy of the Water/Silica Interface: Screening and Interference. *Phys. Chem. Chem. Phys.* **2017,** *19* (25), 16875-16880.
88. Jena, K. C.; Covert, P. A.; Hore, D. K. The Effect of Salt on the Water Structure at a Charged Solid Surface: Differentiating Second- and Third-Order Nonlinear Contributions. *J. Phys. Chem. Lett.* **2011,** *2* (9), 1056-1061.
89. Jena, K. C.; Hore, D. K. Variation of Ionic Strength Reveals the Interfacial Water Structure at a Charged Mineral Surface. *J. Phys. Chem. C* **2009,** *113* (34), 15364-15372.
90. Covert, P. A.; Jena, K. C.; Hore, D. K. Throwing Salt into the Mix: Altering Interfacial Water Structure by Electrolyte Addition. *J. Phys. Chem. Lett.* **2013,** *5* (1), 143-148.
91. Darlington, A. M.; Jarisz, T. A.; Dewalt-Kerian, E. L.; Roy, S.; Kim, S.; Azam, M. S.; Hore, D. K.; Gibbs, J. M. Separating the pH-Dependent Behavior of Water in the Stern and Diffuse Layers with Varying Salt Conceration. *J. Phys. Chem. C* **2017**.
92. Dewan, S.; Yeganeh, M. S.; Borguet, E. Experimental Correlation between Interfacial Water Structure and Mineral Reactivity. *J. Phys. Chem. Lett.* **2013,** *4* (11), 1977-1982.
93. Darlington, A. M.; Jarisz, T. A.; DeWalt-Kerian, E. L.; Roy, S.; Kim, S. H.; Azam, M. S.; Hore, D. K.; Gibbs, J. M. Separating the pH-Dependent Behavior of Water in the Stern and Diffuse Layers with Varying Salt Concentration. *J. Phys. Chem. C* **2017,** *121*, 20229-20241.
94. Garcia Rey, N.; Weissenborn, E.; Schulze-Zachau, F.; Gochev, G.; Braunschweig, B. Quantifying Double-Layer Potentials at Liquid–Gas Interfaces from Vibrational Sum-Frequency Generation. *J. Phys. Chem. C* **2019,** *123* (1279-86).
95. Zhao, X.; Ong, S.; Wang, H.; Eisenthal, K. B. New Method for Determination of Surface pKa Using Second Harmonic Generation. *Chem. Phys. Lett.* **1993,** *214* (2), 203-207.

96. Zhao, X.; Ong, S.; Eisenthal, K. B. Polarization of Water Molecules at a Charged Interface. Second Harmonic Studies of Charged Monolayers at the Air/Water Interface. *Chem. Phys. Lett.* **1993,** *202* (6), 513-520.
97. Hayes, P. L.; Malin, J. N.; Jordan, D. S.; Geiger, F. M. Get Charged Up: Nonlinear Optical Voltammetry for Quantifying the Thermodynamics and Electrostatics of Metal Cations at Aqueous/Oxide Interfaces. *Chem. Phys. Lett.* **2010,** *499* (4), 183-192.
98. Geiger, F. M. Second Harmonic Generation, Sum Frequency Generation, and $\chi^{(3)}$: Dissecting Environmental Interfaces with a Nonlinear Optical Swiss Army Knife. *Annu. Rev. Phys. Chem.* **2009,** *60* (1), 61-83.
99. Walker, D. S.; Richmond, G. L. Depth Profiling of Water Molecules at the Liquid−Liquid Interface Using a Combined Surface Vibrational Spectroscopy and Molecular Dynamics Approach. *J. Am. Chem. Soc.* **2007,** *129* (30), 9446-9451.
100. Pezzotti, S.; Galimberti, D. R.; Shen, Y. R.; Gaigeot, M.-P. Structural Definition of the BIL and DL: A New Universal Methodology to Rationalize Non-Linear $\chi^{(2)}(\omega)$ SFG Signals at Charged Interfaces, Including $\chi^{(3)}(\omega)$ Contributions. *Phys. Chem. Chem. Phys.* **2018,** *20* (7), 5190-5199.
101. Pfeiffer-Laplaud, M.; Gaigeot, M.-P. Electrolytes at the Hydroxylated (0001) α-Quartz/Water Interface: Location and Structural Effects on Interfacial Silanols by DFT-Based MD. *J. Phys. Chem. C* **2016,** *120* (26), 14034-14047.
102. Steel, W. H.; Lau, Y. Y.; Beildeck, C. L.; Walker, R. A. Solvent Polarity across Weakly Associating Interfaces. *J. Phys. Chem. B* **2004,** *108* (35), 13370-13378.
103. Bon, V.; Klein, N.; Senkovska, I.; Heerwig, A.; Getzschmann, J.; Wallacher, D.; Zizak, I.; Brzhezinskaya, M.; Mueller, U.; Kaskel, S. Exceptional Adsorption-Induced Cluster and Network Deformation in the Flexible Metal-Organic Framework DUT-8(Ni) Observed by *in situ* X-ray Diffraction and EXAFS. *Phys. Chem. Chem. Phys.* **2015,** *17*, 17471.
104. Ohno, P. E.; Chang, H.; Spencer, A. P.; Boamah, M. D.; Liu, Y.; Wang, H.-f.; Geiger, F. M. Beyond the Gouy-Chapman Model with Heterodyne-Detected Second Harmonic Generation. *chemRxiv* **2019**.
105. Boamah, M. D.; Ohno, P. E.; Geiger, F. M.; Eisenthal, K. B. Relative Permittivity in the Electrical Double Layer from Nonlinear Optics. *J. Chem. Phys.* **2019,** *148* (22), 222808.
106. Reddy, S. K.; Thiraux, R.; Wellen Rudd, B. A.; Lin, L.; Adel, T.; Joutsuka, T.; Geiger, F. M.; Allen, H. C.; Morita, A.; Paesani, F. Bulk Contributions Modulate the Sum-Frequency Generation Spectra of Water on Model Sea-Spray Aerosols. *Chem* **2018,** *4*, 1629-44.
107. Proetto, M. T.; Rush, A. M.; Chien, M. P.; Abellan Baeza, P.; Patterson, J. P.; Thompson, M. P.; Olson, N. H.; Moore, C. E.; Rheingold, A. L.; Andolina, C., et al. Dynamics of Soft Nanomaterials Captured by Transmission Electron Microscopy in Liquid Water. *J. Am. Chem. Soc.* **2014,** *136* (4), 1162-5.
108. Parent, L. R.; Bakalis, E.; Ramirez-Hernandez, A.; Kammeyer, J. K.; Park, C.; de Pablo, J.; Zerbetto, F.; Patterson, J. P.; Gianneschi, N. C. Directly Observing Micelle Fusion and Growth in Solution by Liquid-Cell Transmission Electron Microscopy. *J. Am. Chem. Soc.* **2017,** *139* (47), 17140-17151.

**Table 1.** Summary of $d_h$ and ξ-potential of extruded vesicles diluted to 10 μg $mL^{-1}$ in 2 mM HEPES at pH 7.4. Ionic strength was adjusted using NaCl.

| | **$d_h$ (nm)** | | **ξ-potential (mV)** | |
|---|---|---|---|---|
| | **1 mM NaCl** | **25 mM NaCl** | **1 mM NaCl** | **25 mM NaCl** |
| **POPC** | 100 ± 10 | 93 ± 3 | – 11 ± 3 | – 6 ± 2 |
| **8:2 POPC:rLPS** | 93 ± 3 | 87 ± 2 | – 12 ± 4 | – 5 ± 3 |
| **8:2 POPC:sLPS** | 108 ± 6 | 104 ± 4 | – 10 ± 2 | – 7 ± 2 |
| **rLPS** | 75 ± 4 | 70 ± 3 | – 6.1 ± 0.9 | – 9 ± 2 |

**Scheme 1.** Structures of A) POPC, B) rough LPS (rLPS), and C) smooth LPS (sLPS) studied herein.

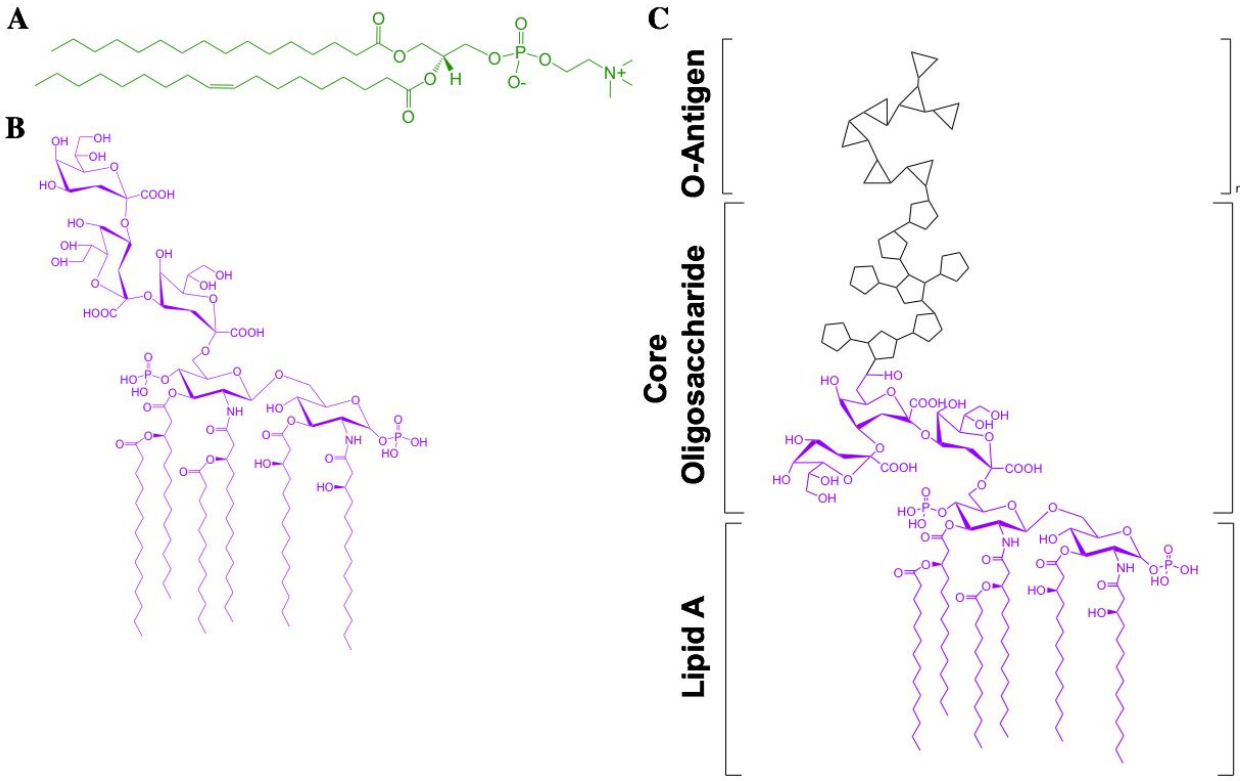

**Scheme 2.** Cartoon of 8:2 POPC:rLPS bilayer showing possible binding sites of nickel cations to an rLPS-containing lipid bilayer membrane.

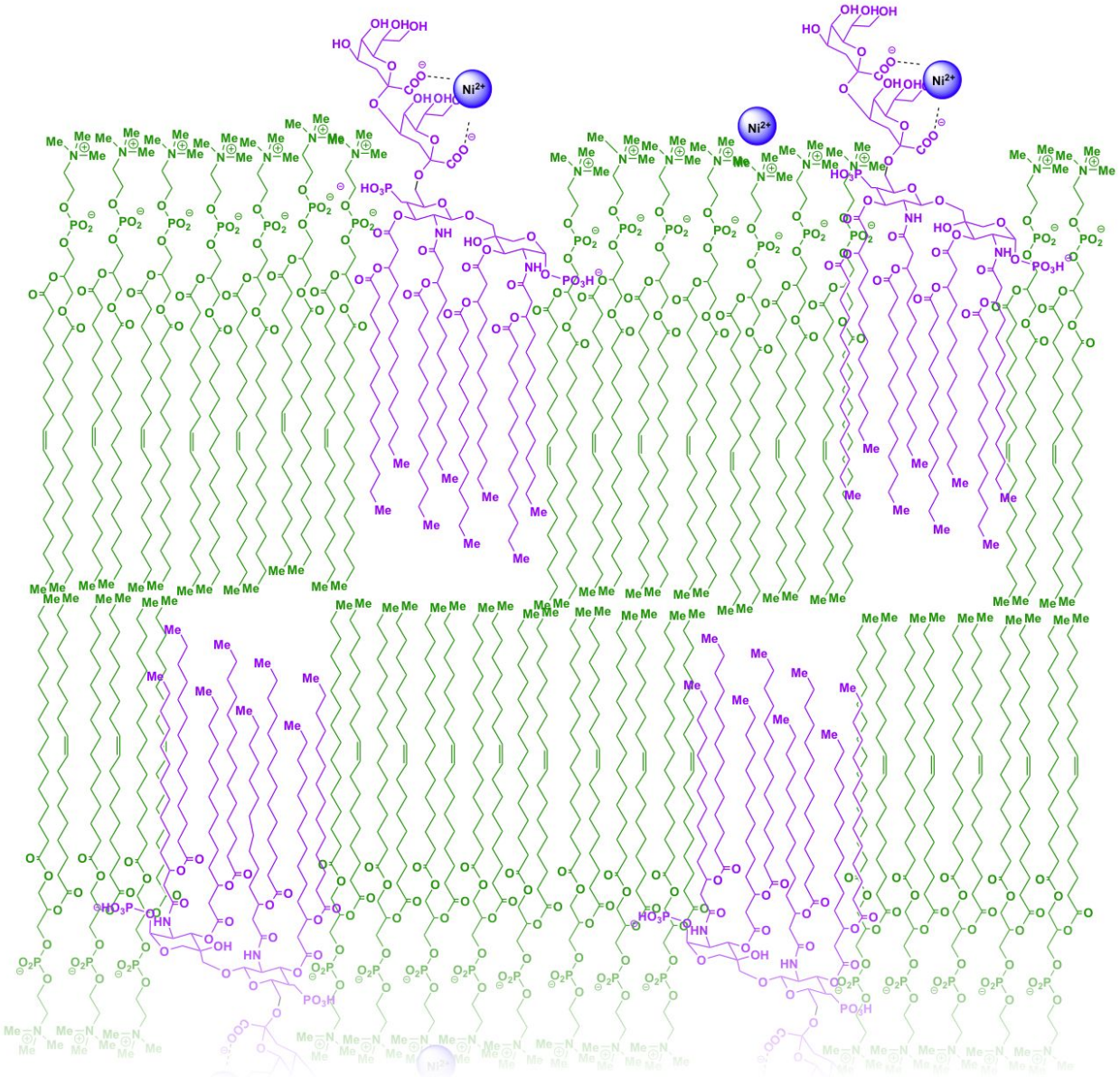

**Figure 1.** CryoTEM images of vesicles studied herein and their interactions with nickel ions. Scale bar is 200 nm.

**Figure 2.** A) Hydrodynamic diameter ($d_h$) and B) $\xi$-potential measurements of vesicles as a function of concentration of $NiCl_2$. Error bars are obtained by averaging 30 runs of 3 different solutions. These measurements were taken in 25 mM NaCl:2 mM HEPES at pH 7.4 to mimic the SHG experimental conditions. POPC (green circle), 8:2 POPC:rLPS (purple circle), and 8:2 POPC:sLPS (grey circle), rLPS (purple triangle).

**Figure 3.** A) Corrected $I_{SHG}$ from charge screening experiments and B) Langmuir adsorption isotherms on POPC (green circle), 8:2 POPC:rLPS (purple circle), and 8:2 POPC:sLPS (grey circle). Charge screening and adsorption experiments are done with background 2 mM HEPES with varying NaCl concentrations and 25 mM NaCl:2 mM HEPES with varying $NiCl_2$ concentrations, respectively, at pH 7.4.

**Figure 4.** A) Reversibility of nickel adsorption with increasing nickel concentration, B) on-off trace of 100 mM $NiCl_2$ adsorption, and C) hysteresis of $NiCl_2$ adsorption on 8:2 POPC:sLPS. Each letter in the plot represents A) bare lipid bilayer, B) 1 mM $NiCl_2$, C) nickel free buffer solution, D) 10 mM $NiCl_2$, and E) 100 mM $NiCl_2$. The background buffer solution was 25 mM NaCl:2 mM HEPES at pH 7.4. Right-axis of Figure 5A and 5B are measured reference laser power.

**Figure 5.** XPS spectrum of bare 8:2 POPC:sLPS that was never exposed to $NiCl_2$ (grey) overlaid with that of 8:2 POPC:sLPS exposed to 100 mM $NiCl_2$ and rinsed with nickel-free buffer (green). The spectra have been background subtracted.

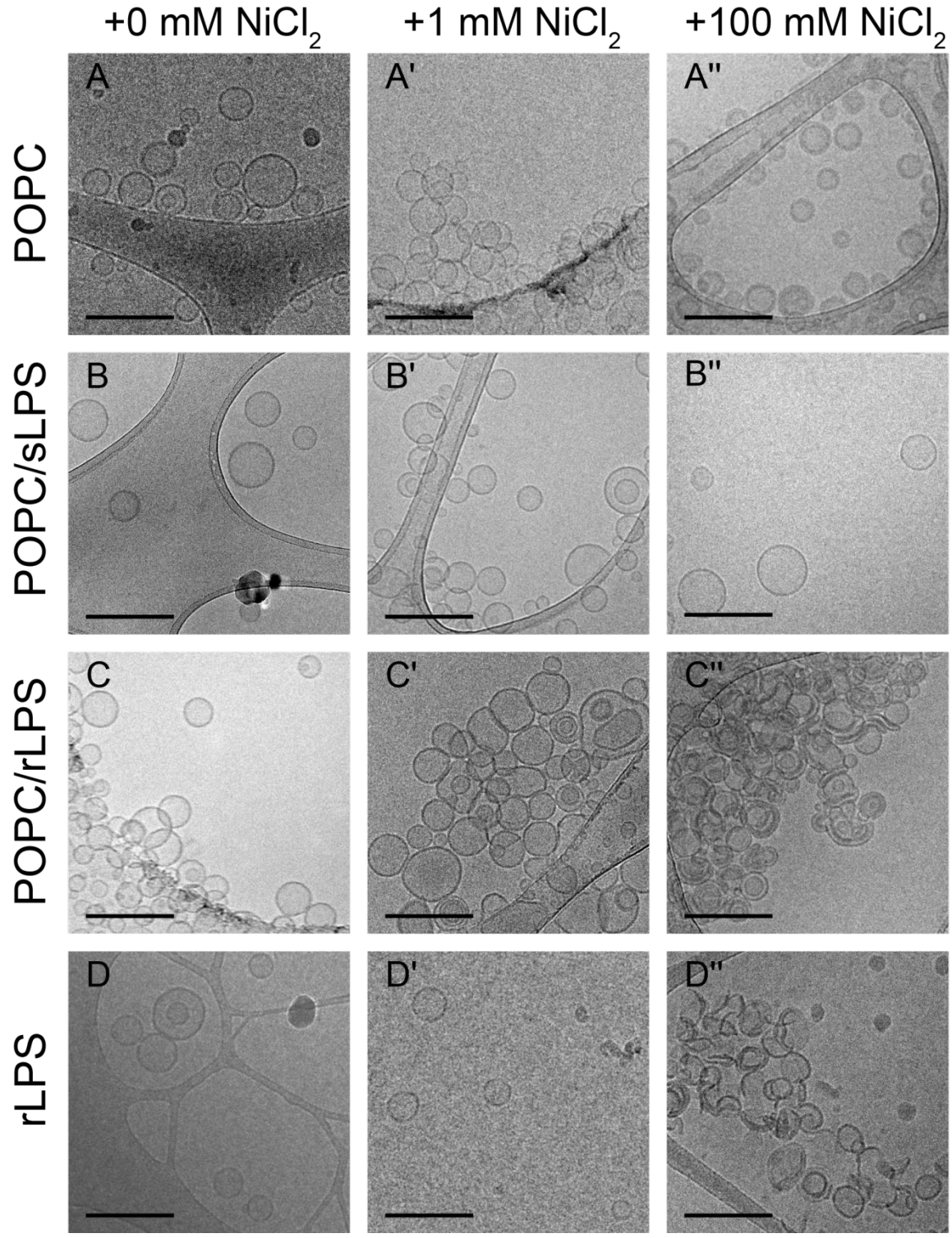
+0 mM NiCl2
+1 mM NiCl2
+100 mM NiCl2
POPC
POPC/sLPS
POPC/rLPS
rLPS
A
A'
A"
B
B'
B"
C
C'
C"
D
D'
D"

**Figure 1.**

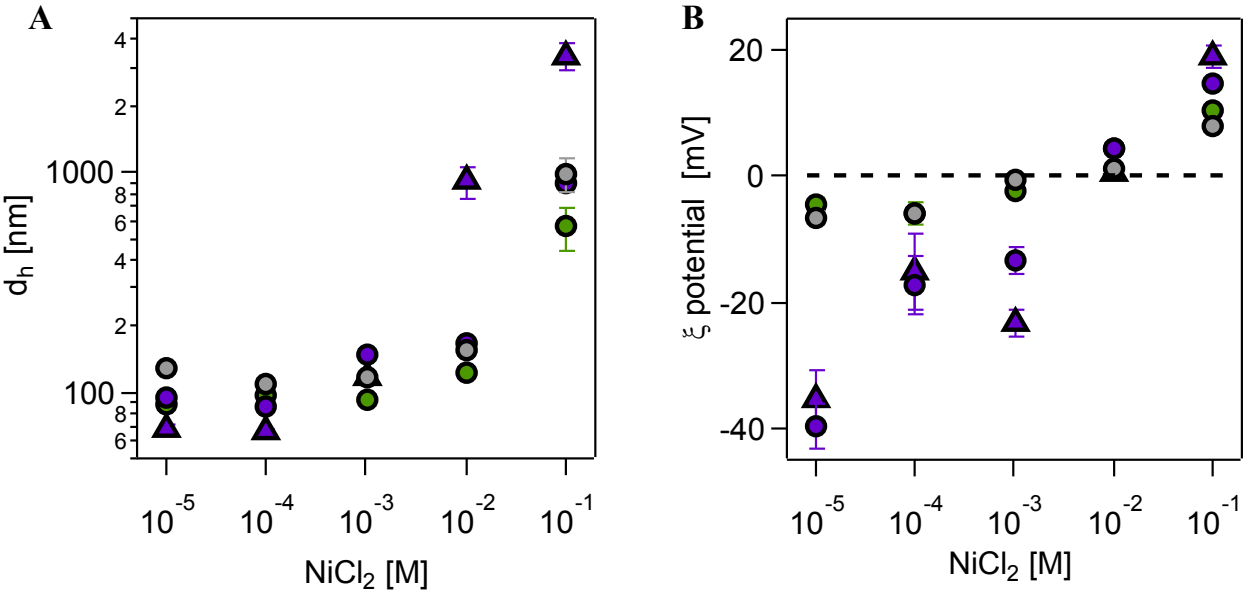


**Figure 2.**

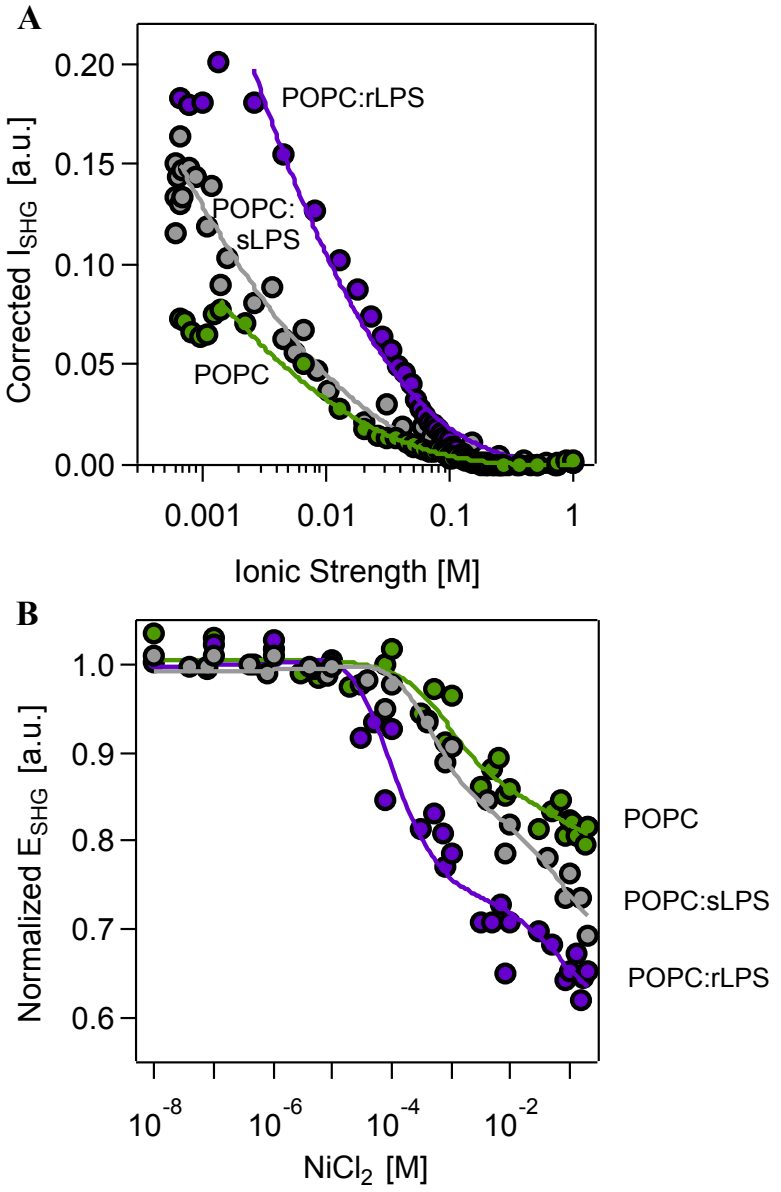
A
0.20
0.15
0.10
0.05
0.00
Corrected $I_{SHG}$ [a.u.]
POPC:rLPS
POPC:
sLPS
POPC
0.001
0.01
0.1
1
Ionic Strength [M]
B
1.0
0.9
0.8
0.7
0.6
Normalized $E_{SHG}$ [a.u.]
POPC
POPC:sLPS
POPC:rLPS
$10^{-8}$
$10^{-6}$
$10^{-4}$
$10^{-2}$
$NiCl_2$ [M]

**Figure 3.**

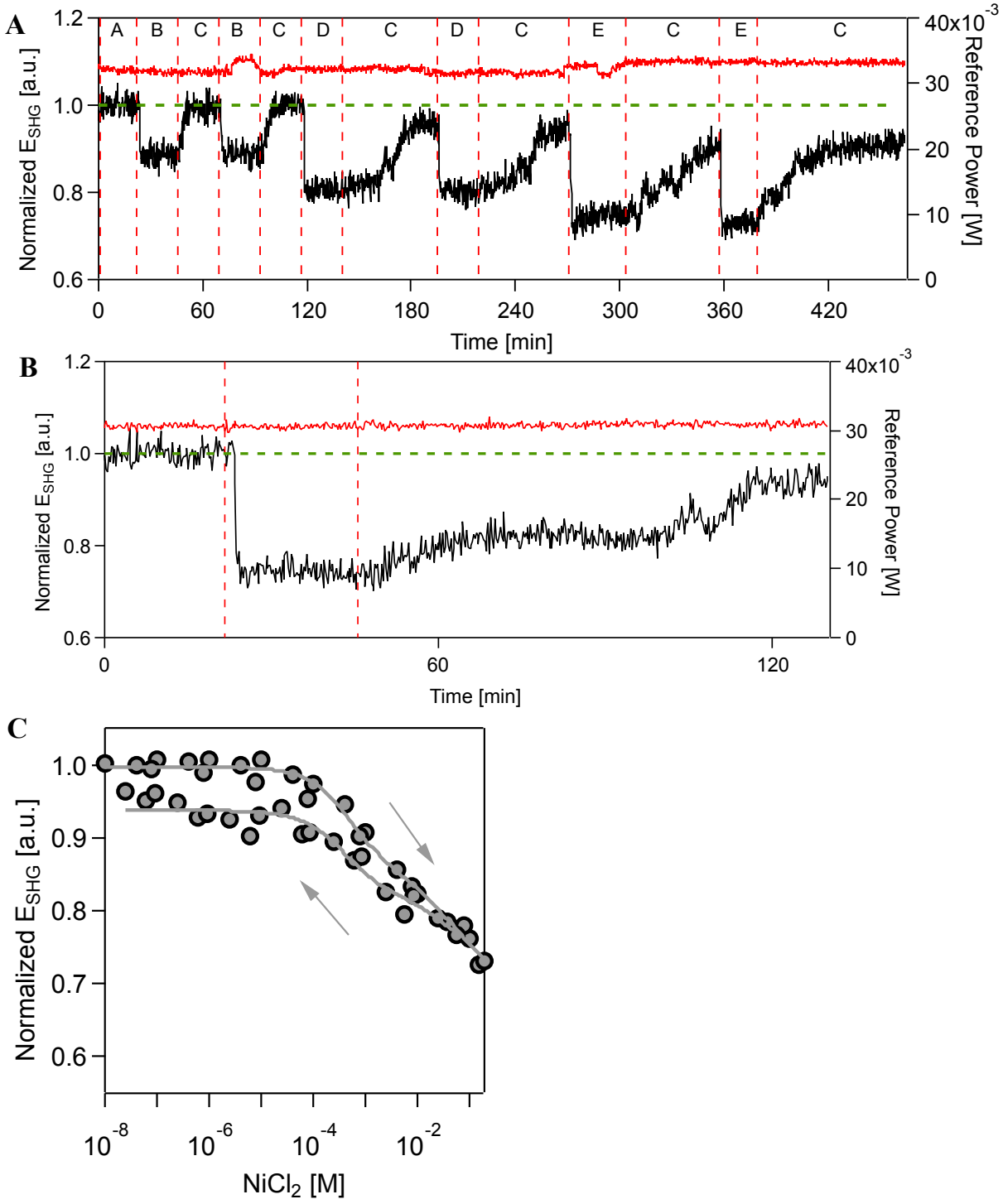
A
A B C B C D C D C E C E C
Normalized $E_{SHG}$ [a.u.]
Reference Power [W]
40x10$^{-3}$
Time [min]
B
Normalized $E_{SHG}$ [a.u.]
Reference Power [W]
40x10$^{-3}$
Time [min]
C
Normalized $E_{SHG}$ [a.u.]
$NiCl_2$ [M]

**Figure 4.**

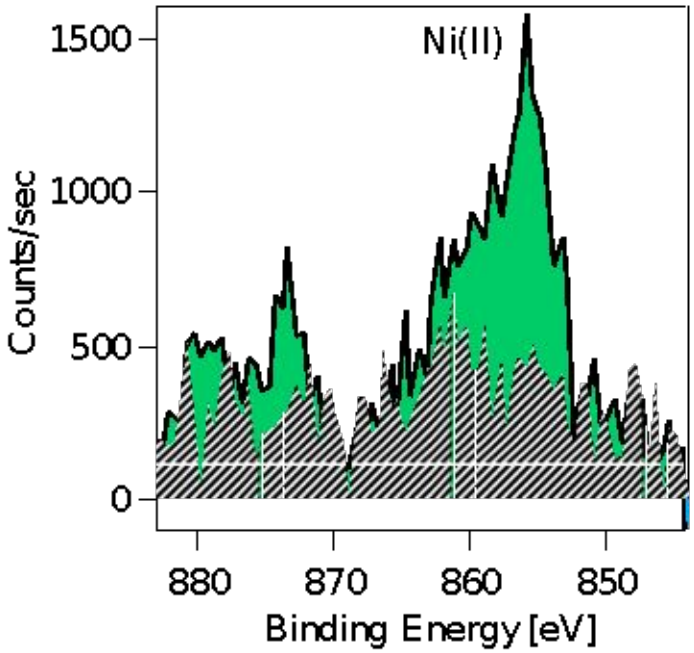
Ni(II)
1500
1000
500
0
Counts/sec
880
870
860
850
Binding Energy [eV]

**Figure 5.**

**TOC Graphic.**